

Autoignition of isolated *n*-heptane droplets in air and hot combustion products at microturbine conditions

J. Wang and E. Mastorakos

Department of Engineering, University of Cambridge, Cambridge CB2 1PZ, UK

ARTICLE HISTORY

Compiled January 24, 2022

ABSTRACT

Spontaneous ignition of isolated *n*-heptane droplets with initial diameters of 20–100 μm is simulated using air at 4 atm and 700–1200 K, which includes the typical operating conditions of recuperated microturbines. Because some fuel droplets in a combustor may be sprayed or carried to near the recirculation zone, the simulations use a mixture of pure air and hot combustion products as the oxidiser. The flame structures, evaporation times, and autoignition times in both physical and mixture fraction spaces for the different conditions are presented and compared. The variables examined include the air preheat temperature, amount of dilution with hot products, initial fuel droplet diameter, oxidiser temperature, and oxygen concentration. The results show that droplets in pure air at microturbine conditions fully evaporate before ignition, suggesting that a prevapourised concept is suitable for microturbines. The dilution with hot combustion products decreases the ignition delay time mainly by raising the oxidiser temperature. Low-temperature chemistry does not have a significant effect on droplet ignition because adding even a small amount of hot combustion products can increase the oxidiser temperature to higher than the temperatures favorable for low-temperature kinetics. The cool flame is only observed for 100 μm droplets at low temperatures, but two-stage ignition is not observed.

KEYWORDS

Autoignition; single droplet; hot products; low-temperature chemistry; microturbine;

1. Introduction

Gas turbines are often known for being used in large applications such as airplanes and power stations, but the gas turbines with smaller power output—often referred to as microturbines—have many applications as well. For instance, microturbines can be used to power unmanned aerial vehicle [1], to act as the auxiliary power unit (APU) on aircrafts [2], and to supply electricity and heat for buildings [3]. More recently, they have been identified as a promising range extender to charge the battery onboard hybrid electric vehicles *in-situ* [4, 5]. These microturbines range extenders need to operate on common liquid fuels and must comply with the road transportation emission regulations. To achieve similar fuel efficiency to that of other range extenders, such as a piston engine, the microturbine range extenders will need to use a heat exchanger, also known as a recuperator, to enable the exhaust gas to preheat the air

between the compressor and combustor [6, 7]. Therefore, developing the combustion system of microturbines for hybrid electric vehicles requires understanding liquid fuel flames in highly preheated air.

The presence of fuel droplets in combustors can cause additional challenges for controlling the NO_x emissions. When a liquid fuel droplet begins to evaporate, the fuel vapor diffuses into the oxidiser and can result in a diffusion flame in the gaseous phase around the droplet, which is also referred to as droplet combustion. These diffusion flames have high flame temperature and can lead to high thermal NO_x emissions [8]. To avoid droplet burning, some microturbines use lean-premixed-prevaporised (LPP) combustion to prevaporise the fuel before the combustion zone [4, 9, 10]. More recently, moderate or intense low-oxygen dilution (MILD) combustion—a combustion mode that dilutes air and fuel with recirculating hot combustion products to maintain a low peak flame temperature and achieve low emissions [11]—has been proposed and implemented in lab-scale burners [12–14]. Both LPP and MILD technologies can benefit from better understanding the droplet evaporation and autoignition processes.

This study aims to understand droplet evaporation and autoignition in microturbines by simulating a single fuel droplet immersed in either pure air or a mixture of air and hot combustion products. We consider droplets in air diluted with hot products because although all fuel droplets in an ideal LPP combustor would be vaporised before ignition, full prevaporisation is not always achieved in practise [15], and some droplets may be sprayed or carried to near the flame or into the recirculation zone, which can affect the evaporation and autoignition time scales [16]. Therefore, modelling the oxidiser using a mixture of pure air and hot products is useful for both LPP and MILD combustion systems. The results reveal the boundary of possible LPP operation under various mixing conditions and droplet sizes.

Another objective of this paper is to study the effect of low-temperature chemistry, therefore we will use *n*-heptane as the fuel, which is known to exhibit phenomena caused by low-temperature kinetics and is a common surrogate for diesel. Indeed, previous experiments of *n*-heptane droplets with initial diameter of $d_0 = 700\text{--}750\ \mu\text{m}$ in air have observed the common phenomena associated with low-temperature kinetics, such as the cool flame and two-stage ignition [17, 18]. Several single droplet simulations have also modelled the cool flame and two-stage ignition using different chemical mechanisms [19–22]. Unlike homogeneous mixtures of *n*-heptane and air, however, these droplet experiments and simulations did not observe the negative temperature coefficient (NTC) [23]. This work will examine the effect of low-temperature chemistry on droplets in both pure air as well as air diluted by hot products. The simulations are also done using droplets of $d_0 = 20\text{--}100\ \mu\text{m}$ to represent the typical droplet size in engines, which is smaller than many previous studies on single droplet combustion.

This paper explores how *n*-heptane droplet behaves in air preheated to $700\text{--}1200\ \text{K}$ at 4 atm, which covers the typical operating conditions of a recuperated microturbine today [24–26], with an emphasis on the effect of low-temperature chemistry. We will first present the results, in both physical and mixture fraction spaces, for droplets immersed in pure air. Then, the results with hot combustion products added to the oxidiser will be presented. By examining profiles of temperature and mass fractions of several intermediate species, we examine the effect of hot product dilution and droplet size on the reaction pathways and droplet ignition. Lastly, we discuss the influence of parameters that contribute to droplet ignition. Based on the simulation results, we discuss the suitability of LPP combustion for microturbines and summarise the effect of low-temperature chemistry.

2. Methods

2.1. Numerical simulation and chemical mechanism

The numerical simulation models the behaviour of an isolated n -heptane droplet in a stagnant oxidiser in microgravity. There is no convective motion except for Stefan flow due to droplet evaporation. These conditions and the assumption of spherical symmetry simplify a three-dimensional scenario into a one-dimensional problem. The code solves the unsteady transport equations of mass, energy, and species mass fraction in both gaseous and liquid phases. Heat transfer due to radiation is neglected based on the assumption that its effect on the evaporation process prior to autoignition is insignificant. While radiation may have a small effect when the oxidiser contains more hot combustion products, it is still unlikely to substantially change the results and trends observed. The full governing equations, interface conditions, and more detailed descriptions of the numerical code can be found in Ref. [20, 27, 28]. This code has also been previously validated against experimental results [20].

The simulation domain is $100r_0$, where r_0 is the initial radius of the droplet. The liquid phase contains 600 equally spaced nodes, whereas the gaseous phase contains 300 nodes that are concentrated towards the droplet surface. The initial droplet diameters are 20, 40, and 100 μm to respectively represent small, medium, and large droplets in gas turbines. The boundary conditions are

$$\begin{array}{lll} r = 0 : & \frac{\partial T_l}{\partial t} = 0 & \frac{\partial Y_l}{\partial t} = 0 \\ r = r_{\max} : & T_g = T_{g,0} & Y_{g,i} = Y_{g,i,0}. \end{array}$$

The initial droplet temperature, $T_{l,0}$, is 340 K in all simulations. The combustor inlet air varies between 700–1200 K, but this temperature does not always correspond to the actual initial oxidiser temperature in the simulation, due to the dilution with hot combustion products. The values of $T_{g,0}$ and $Y_{g,i,0}$, the initial temperature and mass fraction for species i in the gaseous phase, are explained in more detail in Section 2.3.

The simulations use the n -heptane skeletal mechanism by Liu et al. [29]. It has 44 species and 185 individually counted forward and backward reactions. This mechanism is chosen for its good agreement with experimental results over a wide range of temperatures, pressures, and equivalence ratios. It includes low-, intermediate-, and high-temperature kinetics to model the multistage ignition phenomena. The chemical reactions can be turned on or off in the simulations to study their effect. The computational time varies for different conditions, with majority of the simulations requiring less than an hour to be completed using a standard computer. This low computational cost allows a wide range of conditions to be studied.

2.2. Postprocessing

Analysing solutions in mixture fraction space is instructive and useful for modelling. The mixture fraction used in this paper is calculated from the Bilger definition [30, 31]. As explained in previous papers [16, 20], the mixture fraction, ξ , of a fuel C_mH_n can be calculated from

Table 1. Temperature and composition of pure air and hot combustion products.

| T_{air} [K] | T_{ox} [K] | Y_{O} | Y_{O_2} | Y_{OH} | $Y_{\text{H}_2\text{O}}$ | Y_{CO} | Y_{CO_2} |
|----------------------|---------------------|----------------|------------------|-----------------|--------------------------|-----------------|-------------------|
| 700 | 2003 | 0.00005 | 0.08937 | 0.00065 | 0.05466 | 0.00018 | 0.11736 |
| 800 | 2076 | 0.00009 | 0.08930 | 0.00092 | 0.05450 | 0.00032 | 0.11713 |
| 900 | 2148 | 0.00015 | 0.08924 | 0.00126 | 0.05428 | 0.00055 | 0.11678 |
| 1000 | 2220 | 0.00024 | 0.08920 | 0.00169 | 0.05400 | 0.00090 | 0.11622 |

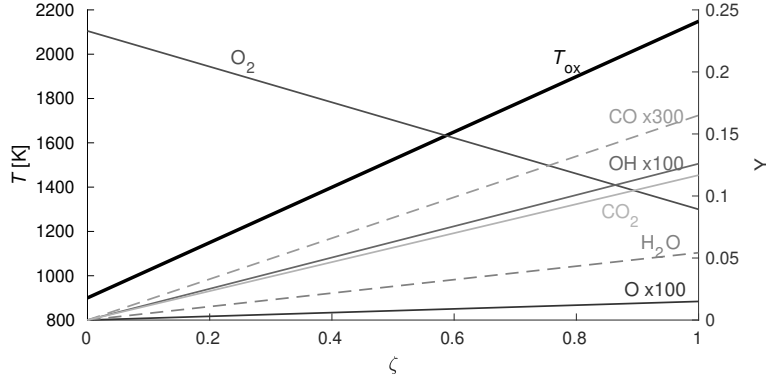


Figure 1. Temperature and composition of mixture of pure air at $T_{\text{air}} = 900$ K and hot combustion products.

$$\xi = \frac{\beta - \beta_0}{\beta_{\text{F}} - \beta_0}$$

$$\beta = \sum_{\alpha=1}^x \left(\frac{a_{\text{C},\alpha}}{m} + \frac{a_{\text{H},\alpha}}{n} - \frac{a_{\text{O},\alpha}}{m + n/4} \right) \frac{Y_{\alpha}}{W_{\alpha}},$$

where β_{F} and β_0 are the β value in the fuel and oxidiser streams, x is the number of species, $a_{A,\alpha}$ is the number of atoms of A in species α , and W is the molecular weight. The scalar dissipation rate is calculated from $N = \frac{\lambda}{\rho c_p} (\nabla \xi \cdot \nabla \xi)$.

The ignition delay time is defined as the time taken for the maximum temperature at any location in space to reach above 2000 K. For cases with initial oxidiser temperature higher than 2000 K, which can occur when the oxidiser is mostly consisted of hot combustion products, the ignition delay time is defined to be the time when maximum dT/dt is observed.

2.3. Oxidiser temperature and composition

Simulations are run for single droplets in different oxidiser temperature and composition to model how the droplet behaves at various locations in the combustor. For instance, the simulations of droplets in pure air represent a droplet in the fresh oxidiser stream. On the other hand, a droplet sprayed close to the recirculation zone of a combustor is represented in simulations with the oxidiser air mixed with hot combustion products.

Following the approach outlined by Giusti et al. [16], the ratio between pure air and hot combustion products is expressed using the dilution variable, ζ , with $\zeta = 0$ representing the pure, undiluted air flowing into the combustion chamber ($Y_{\text{O}_2} = 0.233$ and $Y_{\text{N}_2} = 0.767$), and $\zeta = 1$ being pure hot combustion products. The temperature and

composition of hot combustion products, computed with Cantera [32] at an equivalence ratio of 0.6, at the different air temperatures used in this simulations are listed in Table 1. The conditions between $\zeta = 0$ and $\zeta = 1$ are calculated by adiabatically mixing different proportions of the two mixtures, as demonstrated in Fig. 1. Only species with mass fractions above 10^{-5} are included in the droplet simulation.

To avoid confusion, we use T_{air} to describe the temperature of the pure air flowing into the combustor and T_{ox} to denote the temperature of the actual oxidiser in the droplet simulations. For example, if the air flowing into the combustor is at 900 K, and the simulation has a dilution level of $\zeta = 0.5$, then the temperature conditions for this case would be $T_{\text{air}} = 900$ K and $T_{\text{ox}} = 1524$ K.

3. Results and Discussion

3.1. Droplets in pure air

3.1.1. Flame structure

All simulations in this subsection are for droplets in pure air. Fig. 2 shows the profiles of temperature and mass fractions of key species in the gaseous phase in both physical and mixture fraction space, as well as the maximum temperature and species mass fractions as a function of time, for a $d_0 = 100$ μm droplet. The droplet is immersed in pure air at 800 K, but there is a temperature gradient close to the droplet due to the temperature difference between the droplet surface and the oxidising air.

The significance of the low-temperature kinetics can be observed from the mass fraction of ketoheptylperoxide (KET). As explained in Ref. [29], the low-temperature kinetics begin with a series of chain-propagating reactions and isomerisations that results in the production of KET. The last step in the low-temperature chemistry is the decomposition of KET, which is a chain-branching reaction. Because the decomposition of KET requires relatively high activation energy, a buildup of KET should be observed as low-temperature chemistry proceeds.

The high mass fraction of KET is observed at a location with a relatively low temperature, i.e. closer to the droplet surface and at a higher mixture fraction. The KET mass fraction peaks at 12 ms, which correspond to spikes in the maximum temperature and heat release rate (HRR) that indicate the appearance of a cool flame. In mixture fraction space, KET begins building up at a relatively lean mixture fraction and then shifts towards the fuel-rich direction. These observations are consistent with the results from Borghesi et al., who modelled *n*-heptane droplet ignition using a different mechanism [20].

In addition to low-temperature reactions, H_2O_2 , a species indicative of intermediate-temperature chemistry, as well as CH_2O also slowly accumulate at a leaner mixture fraction. The HRR spikes with the appearance of the cool flame and peaks again at the end of the simulation. Since HRR is calculated per unit area, its sharp increase at the end of the simulation is due to the droplet surface area reducing to zero and does not suggest that any significant heat release is taking place. Like the majority of the simulations using pure air in this study, the droplet finishes evaporating without igniting a hot flame.

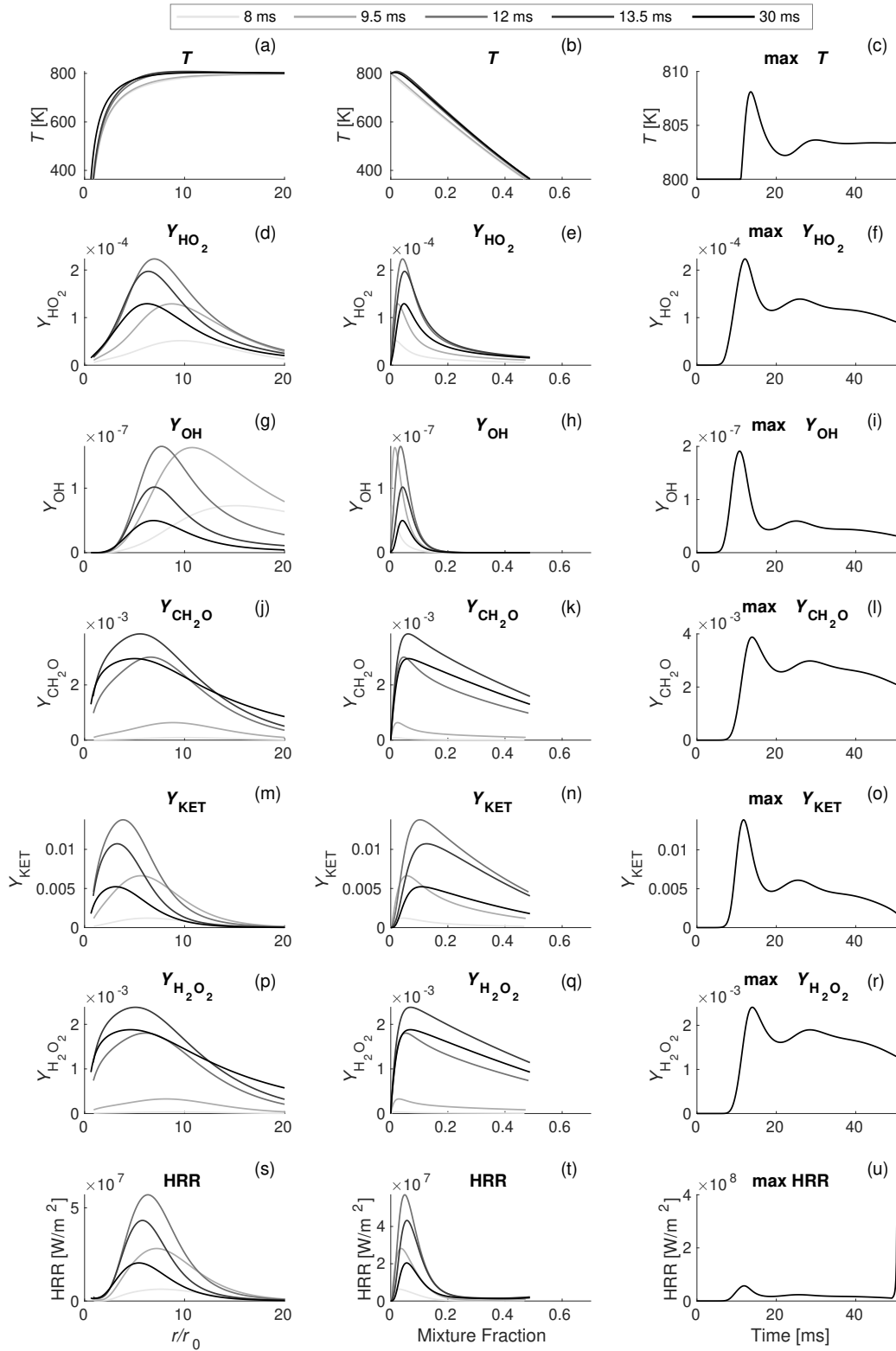


Figure 2. Profiles of temperature, mass fractions of key species, and heat release rate (HRR) in physical space (left) and mixture fraction space (centre) for $d_0 = 100 \mu\text{m}$ and pure air at 800 K. The maximum temperature, mass fractions, and HRR are also plotted over time (right).

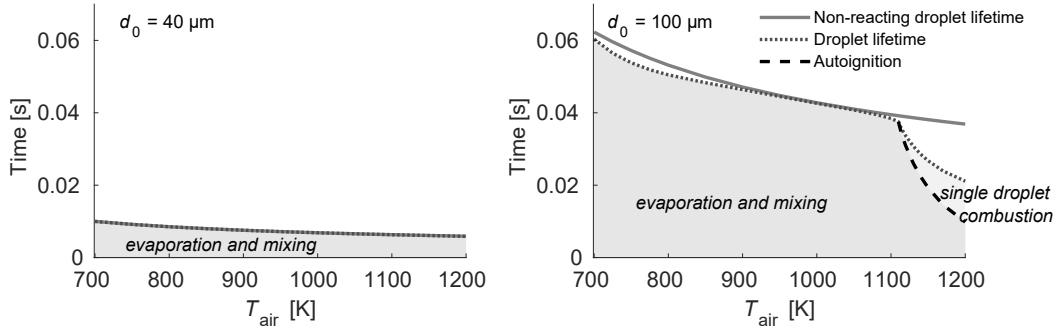


Figure 3. Ignition delay time and droplet lifetime for the $d_0 = 40$ and $100 \mu\text{m}$ cases in pure air.

3.1.2. Autoignition and droplet lifetime

The ignition delay times and the evaporation times of $d_0 = 40$ and $100 \mu\text{m}$ droplets in pure air of 700–1200 K are summarized in Fig. 3. The $d_0 = 40 \mu\text{m}$ droplets completely evaporate before ignition. When the droplet diameter increases to $100 \mu\text{m}$, however, the droplet ignites when immersed in air at temperatures above 1110 K. The trend of larger droplets requiring a lower minimum air temperature to autoignite has also been observed in simulations of ethanol droplets by Millán et al [33]. This difference in behaviour demonstrates that the establishment of a prevapourised combustion system (i.e. no droplet-scale combustion) will depend on conforming to certain boundaries in terms of temperature and droplet size.

Fig. 3 also shows the non-reacting droplet lifetime that is determined by turning off the chemical reactions. At low temperatures, the $d_0 = 100 \mu\text{m}$ droplets evaporate faster when chemical reactions are turned on. This difference between the reacting and non-reacting droplet lifetimes can be attributed to the cool flame that occurs due to low-temperature chemistry. The presence of the cool flame slightly increases the temperature near the droplet surface, as shown in Fig. 2, which results in a small increase in evaporation rate of the droplet. Despite the presence of the cool flame, the $d_0 = 100 \mu\text{m}$ droplets in low-temperature air still completely evaporate without the appearance of a hot flame.

At temperatures high enough for hot flame to occur, the droplet lifetime is significantly shorter with the chemical reactions on. This difference in droplet lifetime can be attributed to the presence of the hot flame around the droplet that increases the evaporation rate. No difference is found in the droplet lifetime with the chemical reactions on and off for $d_0 = 40 \mu\text{m}$, and neither a cool flame nor hot flame is observed. The effect of the initial droplet diameter will be further discussed in Section 3.3.

3.2. Droplets in air diluted with hot products

3.2.1. Flame structure

Fig. 4 shows the typical structure of a hot flame for a case with hot product dilution. The case shown has the same initial conditions as the case in Fig. 2, except 40% of the pure air has been replaced with hot combustion products. Comparing the two figures reveals key differences in their reaction pathways. The $\zeta = 0$ case in Fig. 2 has high levels of KET mass fraction and has a cool flame. For the $\zeta = 0.4$ case, however,

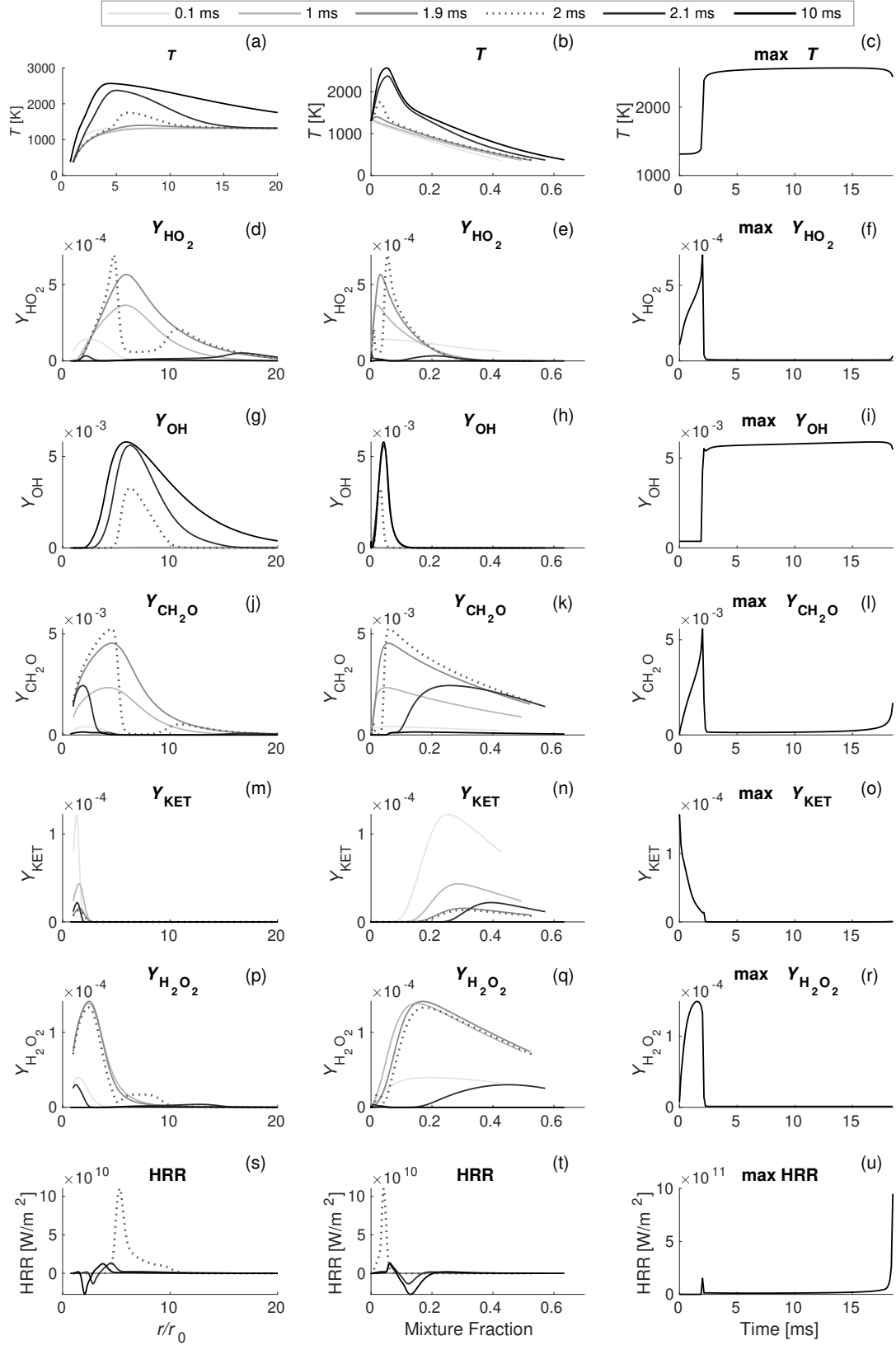


Figure 4. Profiles of temperature, mass fractions of key species, and heat release rate (HRR) in physical space (left) and mixture fraction space (centre) for $d_0 = 100 \mu\text{m}$, $T_{\text{air}} = 800 \text{ K}$, and $\zeta = 0.4$. The maximum temperature, mass fractions, and HRR are also plotted over time (right).

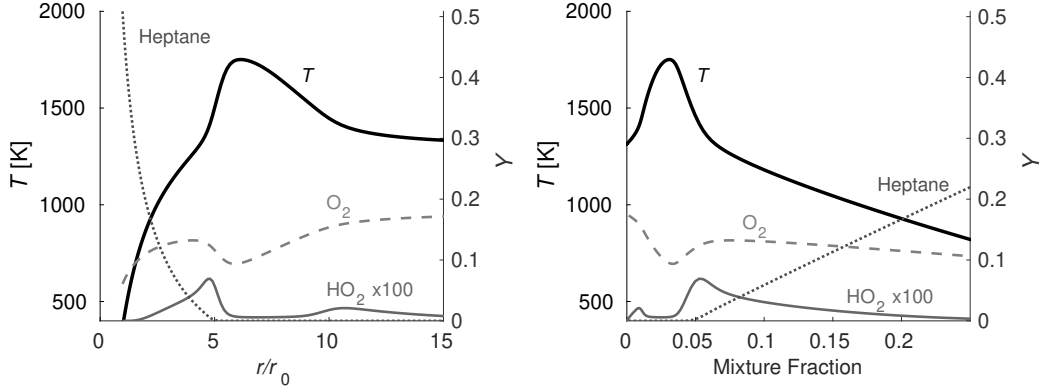


Figure 5. Profiles of temperature and mass fractions of key species in physical space (left) and mixture fraction space (right) for $d_0 = 100 \mu\text{m}$, $T_{\text{air}} = 800 \text{ K}$, $\zeta = 0.4$, and $t = 2 \text{ ms}$.

KET is only found at the start of the simulation, and its maximum mass fraction is approximately two orders of magnitude smaller than that at $\zeta = 0$. The small amount of KET suggests that low-temperature chemistry is not as significant at $\zeta = 0.4$, which is likely because the dilution with hot combustion has raised T_{ox} to 1310 K that is well above the upper temperature limit of low-temperature kinetics.

The $\zeta = 0.4$ case exhibits the single-stage ignition that is typically observed at high initial temperatures. The simulation begins with the production of small amounts of H_2O_2 , HO_2 , and CH_2O , which are then quickly consumed at 2 ms as the hot flame appears. At the same time, the temperature and mass fraction of OH increase quickly near the stoichiometric mixture fraction, which marks the onset of droplet combustion. The profiles of the gas phase temperature as well as the fuel, oxygen, and HO_2 mass fractions at 2 ms are shown in greater detail in Fig. 5. The consumption of HO_2 and O_2 during autoignition can be seen from the dips in the graph, which occur at the same location as the peak in temperature profile. The two peaks in HO_2 mass fraction suggest that two fronts of flame are created, which propagate on either side of ignited region. The flame continues to widen after it is established, and the location of the peak OH and temperature moves to a mixture fraction slightly richer than the stoichiometry. The consistent maximum temperature after the ignition event suggests that the flame remains stable for the rest of the simulation.

3.2.2. Effect of hot products dilution on reaction pathways

Multiple cases with different levels of hot product dilution can be compared in the same figure to further examine the effect of dilution on the reaction pathways. Fig. 6 presents the maximum temperature and mass fraction of key species as a function of time for $T_{\text{air}} = 700 \text{ K}$ at four different levels of dilution. The pure air case ($\zeta = 0$) has the highest mass fractions of KET. As ζ increases, KET production also begins earlier, but the maximum mass fraction of KET is reduced. The reduction in maximum KET mass fraction suggests that low-temperature chemistry is becoming less important as level of dilution increases.

The shift away from low-temperature chemistry can be explained by the high initial oxidiser temperature at high ζ . The relationship between the temperature of the oxidiser and ζ can be observed in the first subplot of Fig. 6. The two-stage ignition region for *n*-heptane at 4 atm is approximately 620–875 K [17]. Thus, diluting the 700 K pure air with even a small amount of hot products at approximately 2000 K may

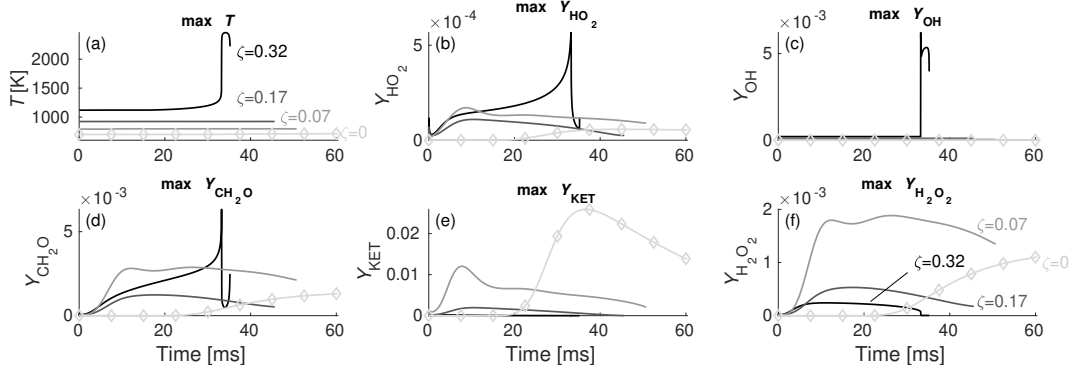


Figure 6. Maximum temperature and species mass fraction as a function of time for $T_{\text{air}} = 700$ K, $d_0 = 100$ μm , and $\zeta = 0, 0.07, 0.17,$ and 0.32 .

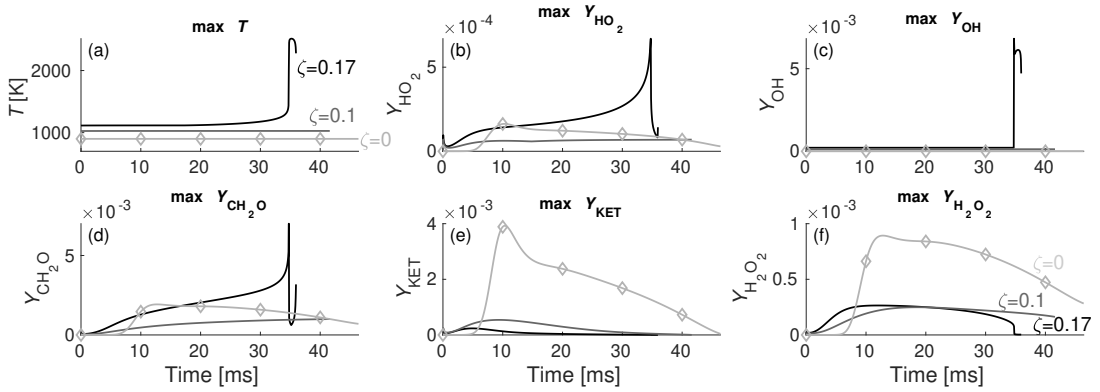


Figure 7. Maximum temperature and species mass fraction as a function of time for $T_{\text{air}} = 900$ K, $d_0 = 100$ μm , and $\zeta = 0, 0.1,$ and 0.17 .

raise the oxidizer temperature above the temperature favorable for low-temperature chemistry. On the other hand, as ζ increases, the productions of H_2O_2 , CH_2O , and HO_2 also begin earlier. At a sufficiently high ζ , which is 0.32 for $T_{\text{air}} = 700$ K, hot-flame ignition is observed. No two-stage ignition is seen because at ζ high enough for hot flame ignition, the initial oxidiser temperature is already above the temperature favorable for low-temperature chemistry.

Fig. 7 presents the results for $T_{\text{air}} = 900$ K at different ζ . Significantly small mass fractions of KET are observed in these simulations because they have been conducted at temperatures above the low-temperature kinetics regime. Like in the $T_{\text{air}} = 700$ K cases, the production of other intermediate species begins earlier as ζ increase. The minimum ζ required for autoignition, however, is reduced to 0.17. Comparing the $\zeta = 0.17$ cases in Fig. 6 and 7 reveals differences in the mass fraction of intermediate species. At $T_{\text{air}} = 900$ K, the mass fractions of CH_2O and HO_2 increase with time until they are consumed during ignition. In contrast, the $T_{\text{air}} = 700$ K case does not have the continuous accumulation of these intermediate species. Following an initial increase, the maximum mass fractions of these intermediate species remain relatively constant for the remaining simulation. The maximum temperature also remains the same for the entire simulation, which indicates that autoignition has not occurred.

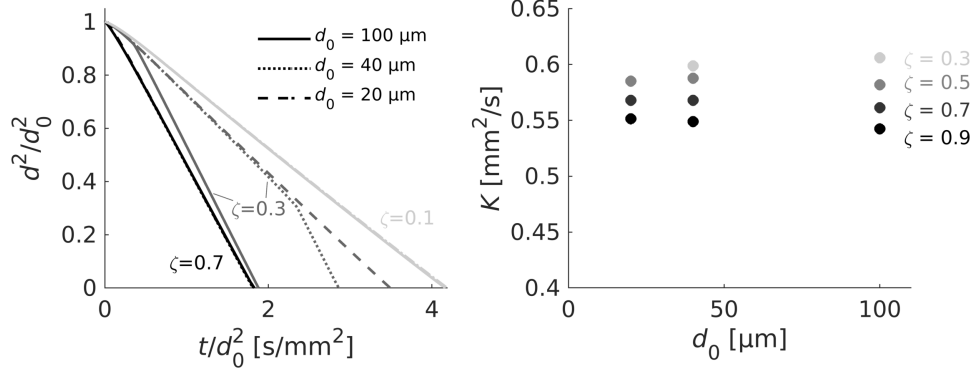


Figure 8. The droplet diameter squared as a function of time (left) and the burning rate after autoignition as a function of initial diameter (right) for $T_{\text{air}} = 900$ K and $\zeta = 0.10 - 0.90$.

3.3. Effect of droplet size

This section explores the behaviours of droplets with different initial diameters. The change in droplet diameter over time is shown in Fig. 8 (left) for $d_0 = 20, 40,$ and 100 μm at $\zeta = 0.1, 0.3,$ and 0.7 . If the droplet combustion proceeds according to the d^2 -law, which states that $d^2/d_0^2 = 1 - Kt/d_0^2$, then the slope of the line would be the burning rate, K . At $\zeta = 0.1$, the droplets evaporate with no autoignition observed (known from the unchanged temperature field that is not shown here). At $\zeta = 0.3$, the smallest droplet also does not autoignite, but the slope of the line is steeper than the $\zeta = 0.1$ case, indicating that the droplet is evaporating faster, which is likely due to the higher oxidiser temperature at the higher ζ . The larger droplets at $\zeta = 0.3$ both see a sharp change in slope, which corresponds to the autoignition event that contributes to the faster evaporation. At $\zeta = 0.7$, autoignition occurs shortly after the start of the simulation, thus there is no noticeable change in slope. Fig. 8 (right) shows the burning rate after autoignition at different initial diameters and various ζ . As ζ increases, K decreases, which can also be observed in the steeper slope of the $\zeta = 0.3$ case comparing to the $\zeta = 0.7$ case on Fig. 8 (left). There are also differences in burning rate for different initial diameters, but Fig. 8 (left) shows that these differences in slopes for the same initial diameter is relatively small. Since the focus of the paper is on the autoignition transient, the simulation does not consider factors such as heat loss due to radiation, which are less important during ignition transient but more relevant for the burning rate after ignition [34]. Therefore, a deeper analysis on the burning rate at various ζ and d_0 is outside the scope of the paper.

The droplet lifetime and ignition delay time for different ζ and d_0 can be summarised and compared in a regime diagram in Fig. 9, which is similar to the diagrams drawn by Giusti et al. in Ref. [16]. According to the d^2 -law, the relationship between d^2/d_0^2 and tK/d_0^2 does not depend on the initial diameter. Therefore, plotting the non-dimensional time, tK/d_0^2 , should collapse the droplet lifetime curves for different initial diameters onto one line for easy comparison. Though K differs for different d_0 and ζ , for simplicity we follow the approach in Ref. [16] and use the kinematic viscosity of pure air for K . Therefore the regime diagram uses a non-dimensional time of $t\nu_{\text{air}}/d_0^2$, where ν_{air} is the kinematic viscosity of the pure air.

To the left of the dashed autoignition line, droplets will evaporate and mix without a hot flame, though ignition may still occur after evaporation. On the other side, between the dashed autoignition line and the solid droplet lifetime line, is the single

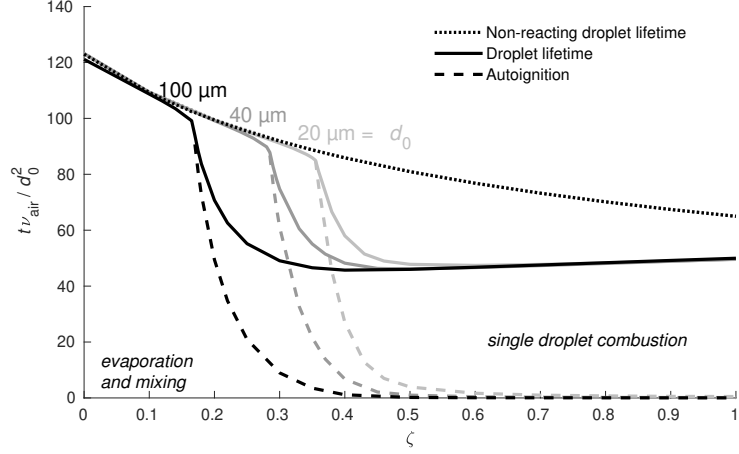


Figure 9. Regime diagram for $T_{\text{air}} = 900$ K and $d_0 = 20, 40,$ and 100 μm .

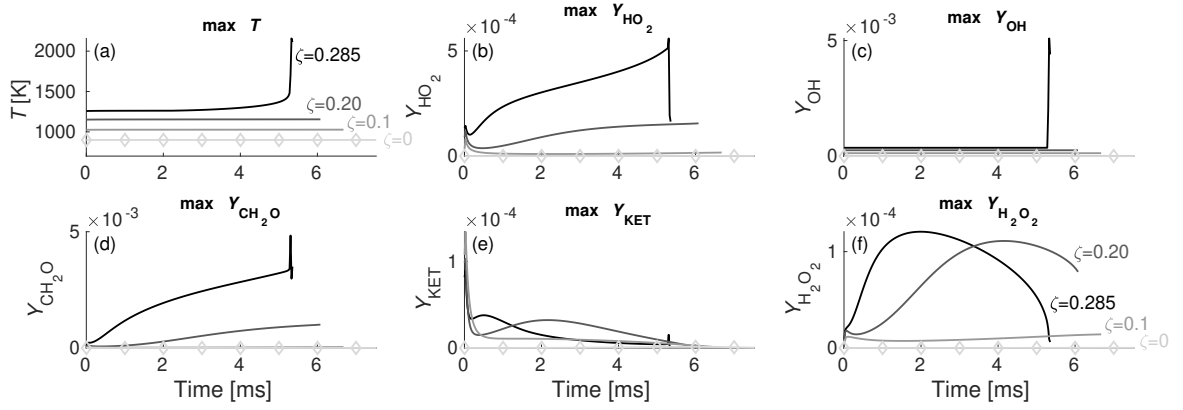


Figure 10. Maximum temperature and species mass fraction as a function of time for $T_{\text{air}} = 900$ K, $d_0 = 40$ μm , and $\zeta = 0, 0.10, 0.20,$ and 0.285 .

droplet combustion zone. The dotted line is the droplet lifetime with chemical reactions turned off. The presence of the hot flame around the droplet decreases the lifetime of the droplet, resulting in the large difference between reacting and non-reacting droplet lifetimes.

As d_0 increases, the single droplet combustion zone in the regime diagram also expands. In other words, large droplets require less hot products present in the oxidiser to autoignite. To further understand the effect of initial droplet diameter, we compare simulation results for $d_0 = 100$ μm in Fig. 7 with the results for a $d_0 = 40$ μm droplet at the same initial conditions, which is shown in Fig. 10. The $d_0 = 40$ μm case at $\zeta = 0$ sees no change in temperature or in the mass fraction of any of the five intermediate species plotted. Similarly, no change is observed at first for the $d_0 = 100$ μm case at $\zeta = 0$. But after the first few uneventful seconds, the levels of intermediate species begin to show more fluctuations, albeit no cool or hot flame is eventually established. Similar observations can be made for the $\zeta = 0.1$ case. In general, increasing d_0 is associated with higher reactivity. At sufficiently high d_0 , droplet ignition will occur.

Fig. 11 further shows the effect of d_0 on ignition. The graph of maximum temperature versus time reveals that droplet ignition occurs for the $d_0 = 500$ and 700 μm cases but not for the $d_0 = 200$ μm case. The observation that larger droplets ignite but the

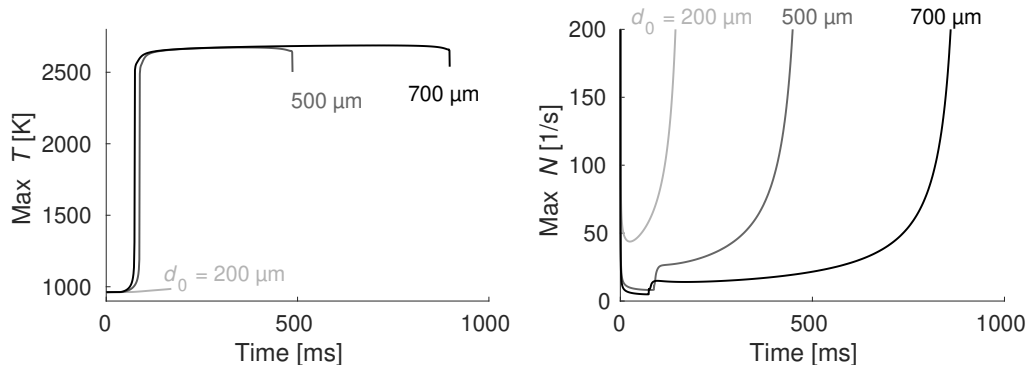


Figure 11. Maximum temperature and scalar dissipation rate as a function of time for $T_{\text{air}} = 700 \text{ K}$, $\zeta = 0.2$, and $d_0 = 200, 500, \text{ and } 700 \mu\text{m}$.

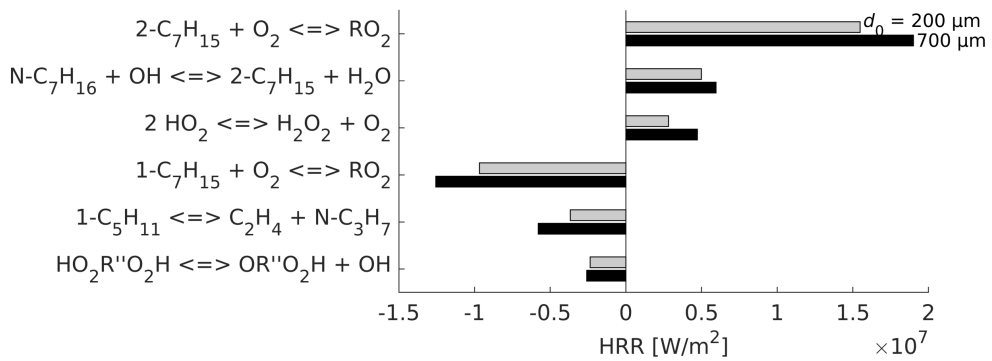


Figure 12. The heat release rate (HRR) of the top 3 exothermic and endothermic reactions at the location of maximum HRR at 50 ms for $d_0 = 200 \text{ and } 700 \mu\text{m}$ at $T_{\text{air}} = 700 \text{ K}$ and $\zeta = 0.2$.

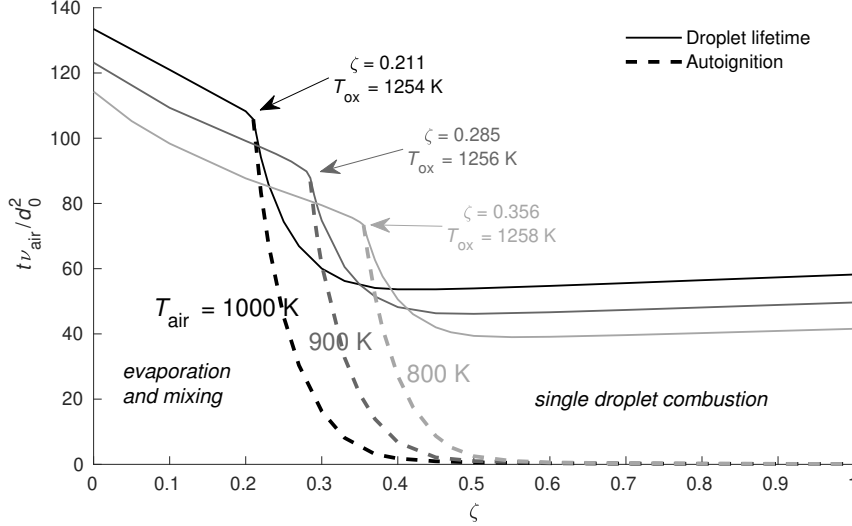


Figure 13. Regime diagram for $d_0 = 40 \mu\text{m}$ and $T_{\text{air}} = 800, 900,$ and 1000 K .

smaller one does not can be explained by Law’s work in 1975 [35]. Law analytically found the Damköhler number—proportional to d_0^2 and defined as the ratio of characteristic flow time to chemical reaction time—critical for droplet ignition. Therefore, the d_0 corresponding to this critical Damköhler number is the minimum d_0 required for droplet ignition to occur. In Fig. 11, the critical d_0 is between 200 and 500 μm .

Fig. 11 also reveals that the $d_0 = 700 \mu\text{m}$ case ignites earlier than the $d_0 = 500 \mu\text{m}$ case. The same graph shows that as d_0 decreases, the maximum scalar dissipation increases. A higher scalar dissipation rate corresponds to a lower Damköhler. Thus, the longer ignition delay time of the $d_0 = 500 \mu\text{m}$ case can be explained by its lower Damköhler, suggesting that the strong diffusion of species is hindering the chemical reaction rate. The difference in chemical reaction rates can be inferred from Fig. 12 that compares the HRR of the top 3 exothermic and endothermic reactions at the location of maximum HRR for $d_0 = 200$ and $d_0 = 700 \mu\text{m}$ before hot flame ignition. The 6 reactions with the largest contribution to the HRR are the same—and many of these reactions are related to low-temperature chemistry and the production of KET (OR''O₂H)—but the amount of heat they release or absorb is greater for the droplet with larger initial diameter. This supports the explanation that larger droplets and lower scalar dissipation rates are associated with higher chemical reaction rates. This phenomenon of a smaller droplet having a longer ignition delay time has been observed and investigated near the ignitable limit in other *n*-heptane droplet simulations and experiments as well [19, 20].

3.4. Effect of pure air temperature

Another regime diagram is shown in Fig. 13 to examine the effect of the air temperature at combustor inlet on a droplet of $d_0 = 40 \mu\text{m}$. As T_{air} increases, single droplet combustion is more likely to occur. Another interpretation is that as T_{air} increases, the minimum ζ needed for single droplet combustion decreases. As noted on Fig. 13, however, these different minimum ζ have similar T_{ox} despite their different mixture composition, which prompts further investigation on the role of oxidiser temperature and composition on droplet ignition.

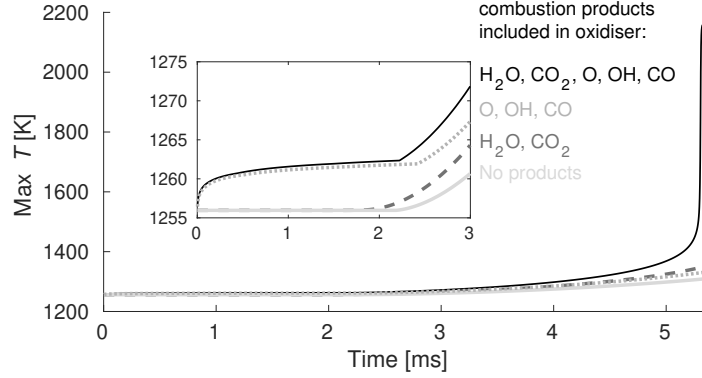


Figure 14. Maximum temperature as a function of time for $d_0 = 40 \mu\text{m}$ and $T_{\text{ox}} = 1256 \text{ K}$. The four mixtures differ in composition but all have the same oxygen content of $Y_{\text{O}_2} = 0.192$.

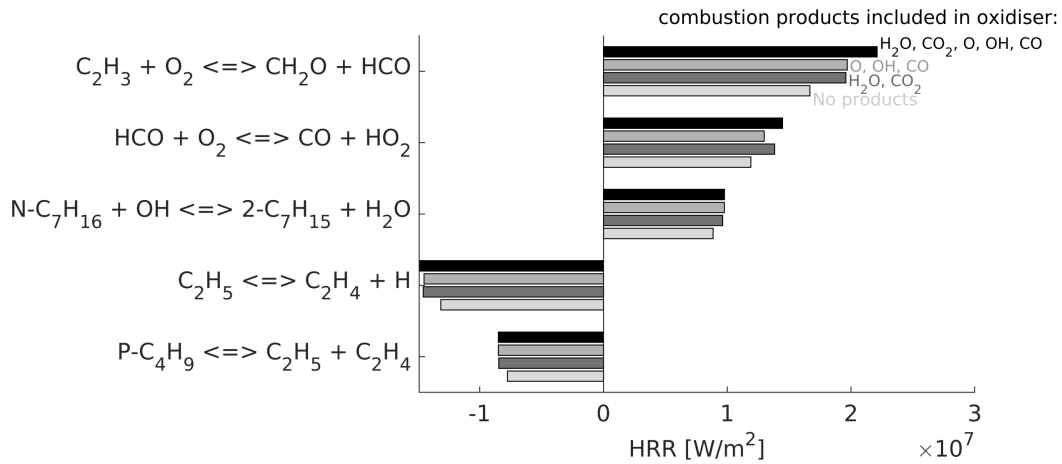


Figure 15. The heat release rate (HRR) of the top 3 exothermic and top 2 endothermic reactions at the location of maximum HRR at 1 ms for $d_0 = 40 \mu\text{m}$ and $T_{\text{ox}} = 1256 \text{ K}$. The four mixtures differ in composition but all have the same oxygen content of $Y_{\text{O}_2} = 0.192$.

The similar minimum ignition temperatures can be explained by the intermediate-temperature reaction pathways. The minimum T_{ox} needed for ignition is well above the two-stage ignition region for *n*-heptane. At these high temperatures, the *n*-heptane droplet bypasses the low-temperature chemistry, as evident from the low levels of KET in Fig. 10. Instead, the droplet exhibits the single-stage intermediate-temperature chemistry dominated ignition [29]. As explained by Westbrook [36], the intermediate-temperature reactions produce H_2O_2 while the temperature slowly increases. Once a critical temperature is reached, H_2O_2 decomposes and produces two OH molecules, which triggers ignition and high-temperature reactions. The decomposition of H_2O_2 is highly sensitive to temperature, which can explain why these systems with different mixture composition have similar minimum T_{ox} for ignition.

Another observation from Fig. 13 is that when the oxidiser contains more combustion products, the minimum T_{ox} needed for ignition is slightly reduced. Increasing the mass fraction of combustion products simultaneously introduces more combustion products and reduces the mass fraction of oxygen. Therefore these two variables are investigated separately.

Fig. 14 presents the maximum temperature over time for four simulations conducted

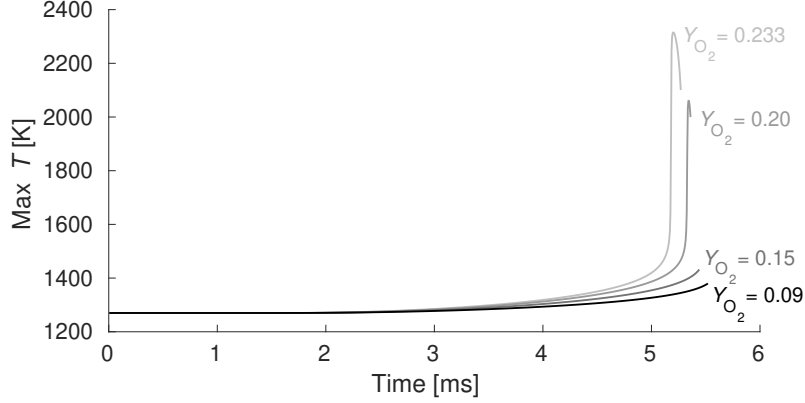


Figure 16. Maximum temperature as a function of time for a droplet of $d_0 = 40 \mu\text{m}$ in gaseous mixture consisted of different ratios of O_2 and N_2 . The initial gaseous temperatures for all cases are $T_{\text{ox}} = 1270 \text{ K}$.

at $T_{\text{ox}} = 1256 \text{ K}$ but with different gaseous mixture compositions. The darkest line represents the case of $T_{\text{air}} = 900 \text{ K}$ and $\zeta = 0.285$ presented in Fig. 10, which includes all main products and intermediate species listed in Table 1. The other three cases exclude either the main products (H_2O and CO_2), the intermediate species (O , OH , CO), or both by replacing them with N_2 .

The case including all main products and intermediate species shows the fastest increase in temperature, and it is the only case that autoignited. The case without any main products or intermediate species shows the slowest rise in temperature. The presence of the intermediate species causes a small initial increases in the maximum temperature, whereas the addition of main products increases the subsequent rate of temperature rise. Thus, having more combustion products in the oxidiser generally decreases the ignition delay time. The results also suggest that when modelling the recirculation zone, it is important to include the intermediate species, even if their mass fraction is relatively small comparing to the main combustion products. Fig. 15 shows HRR of the top 3 endothermic and top 2 exothermic reactions at the location of maximum HRR at 1 ms. Each case has the same set of reactions has the largest contribution to HRR, which suggests that their reaction pathways are similar.

Fig. 16 plots the maximum temperature as a function of time for different ratios of Y_{O_2} and Y_{N_2} at $T_{\text{ox}} = 1270 \text{ K}$. The case with pure air (i.e. $Y_{\text{O}_2} = 0.233$) has the shortest ignition delay time. Fig. 17 shows the HRR of the top exothermic and endothermic reactions at the location of max HRR at 5 ms. The cases with higher Y_{O_2} have significantly higher HRR from the top 2 exothermic reactions that consume O_2 . As Y_{O_2} decreases, the ignition delay time increases. Therefore, all else being equal, cases with lower Y_{O_2} —which occurs when air is diluted with hot products—will require a higher T_{ox} for the droplet to autoignite. But Fig. 13 shows that, when other factors are also considered, more dilution decreases the minimum T_{ox} for ignition. This difference suggests that Y_{O_2} has a much smaller effect on droplet ignition than the oxidiser temperature and the presence of combustion products have.

4. Summary and Conclusions

The evaporation and autoignition processes of *n*-heptane droplets in both pure air and air diluted with hot combustion products are simulated under microturbine operating

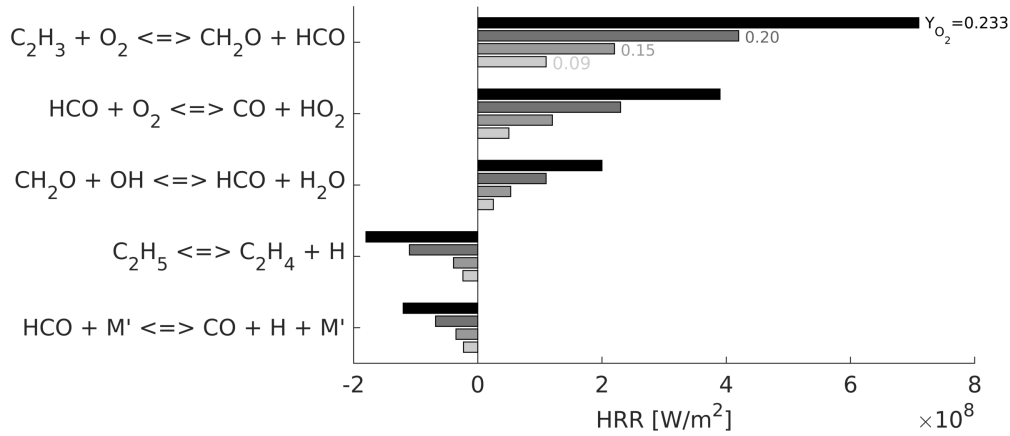


Figure 17. The heat release rate (HRR) of the top 3 exothermic and top 2 endothermic reactions at the location of maximum HRR at 5 ms for $d_0 = 40 \mu\text{m}$ and gaseous mixture consisted of different ratios of O_2 and N_2 . The initial gaseous temperatures for all cases are $T_{\text{ox}} = 1270 \text{ K}$.

conditions. The pure air simulations find that droplets of $d_0 = 40 \mu\text{m}$ completely evaporate before ignition when immersed in air of 700–1200 K. When d_0 is increased to $100 \mu\text{m}$, droplet combustion occurs when air temperature is above 1110 K, which is higher than the current operating temperature of microturbines. The observation that *n*-heptane, a fuel known to autoignite quickly, is able to evaporate before autoignition suggests that the LPP concept is suitable for microturbines. The ignition delay time of droplets, however, can be significantly reduced if the droplet is immersed in air diluted with hot combustion products. These results can help the combustor designer choose the appropriate target for premixer residence time and droplet diameter to avoid droplet combustion.

For every combination of combustor inlet conditions, there is a minimum ζ for droplet ignition to occur. These different minimum ζ values correspond to a similar oxidiser temperature, T_{ox} . This trend suggests that while diluting the air with hot combustion products simultaneously results in higher oxidiser temperature, higher concentration of combustion products, and lower oxygen content, it is the increase in oxidiser temperature that has the largest influence on ignition delay time. This finding suggests that predictions of the onset of droplet combustion will rely on accurate modelling of the temperature of the reacting flow inside the combustor.

Droplet ignition is less likely to occur when the initial diameter of the fuel droplet is small. Smaller droplets have a higher scalar dissipation rate and lower Damköhler number, which implies that the species diffusion dominates and the chemical reactions proceed more slowly. Thus, autoignition of droplets of $d_0 = 20, 40,$ and $100 \mu\text{m}$ is only observed at sufficiently high oxidiser temperatures. At temperatures favourable for low-temperature reaction pathway, the cool flame is only observed for $d_0 = 100 \mu\text{m}$. Even then, due to the combination of short droplet lifetime and high scalar dissipation rate, the cool flame does not lead to two-stage ignition, and thus neither the NTC nor the ZTC is observed.

Given the high temperature of hot combustion products and the relatively narrow range of temperature that is favorable for the cool flame, diluting the pure air even with a small amount of hot combustion products can raise the oxidiser temperature above the low-temperature kinetics limit. Therefore, the effect of low-temperature chemistry

becomes insignificant when the air is diluted with hot combustion products.

Acknowledgement

The authors acknowledge Dr. Giulio Borghesi for the code used to conduct the simulations and Dr. Andrea Giusti for his helpful guidance on using the code.

Funding

The authors acknowledge the financial support from Fonds de Recherche du Quebec – Nature et Technologies and Natural Sciences and Engineering Research Council of Canada.

References

- [1] A. Marcellan, W.P.J. Visser, and P. Colonna, *Potential of Micro Turbine Based Propulsion Systems for Civil UAVs: A Case Study*, Proceedings of ASME Turbo Expo (2016).
- [2] S. Hamilton, *The handbook of microturbine generators*, PennWell, Tulsa, Okla., 2003.
- [3] K. Darrow, R. Tidball, J. Wang, and A. Hampson, *Catalog of CHP Technologies: Section 5. Technology Characterization – Microturbines*, Tech. Rep. March, 2015.
- [4] J. Chen, M.G. Mitchell, and J.G. Nourse, *Development of Ultra-Low Emission Liquid Fuel-Fired Microturbine Engines for Vehicular Heavy Duty Applications*, Proceedings of ASME Turbo Expo (2009).
- [5] A. Karvountzis-Kontakiotis, A.M. Andwari, A. Pesyridis, S. Russo, R. Tuccillo, and V. Esfahanian, *Application of Micro Gas Turbine in Range-Extended Electric Vehicles*, Energy 147 (2018), pp. 351–361.
- [6] G. Xiao, T. Yang, H. Liu, D. Ni, M.L. Ferrari, M. Li, Z. Luo, K. Cen, and M. Ni, *Recuperators for micro gas turbines: A review* (2017).
- [7] J. Ribau, C. Silva, F.P. Brito, and J. Martins, *Analysis of four-stroke, Wankel, and micro-turbine based range extenders for electric vehicles*, Energy Conversion and Management 58 (2012), pp. 120–133.
- [8] A.H. Lefebvre and D.R. Ballal, *Gas turbine combustion: alternative fuels and emissions*, 3rd ed., CRC Press Taylor & Francis Group, 2010.
- [9] P. Johansson, *Development of a Dry Low-NO_x Combustor for the VT100 Automotive Gas Turbine*, Proceedings of ASME Turbo Expo (1997).
- [10] B. Sjoblom and J. Rehn, *The Volvo high speed generation hybrid drive and associated combustion system*, Energy Conversion and Management 38 (1997), pp. 1225–1235.
- [11] A. Cavaliere and M. de Joannon, *Mild Combustion*, Progress in Energy and Combustion Science 30 (2004), pp. 329–366.
- [12] M.C. Cameretti, R. Tuccillo, F. Reale, and R. Piazzesi, *Numerical simulation of liquid bio-fuel combustion in an EGR equipped micro gas turbine*, American Journal of Applied Sciences 12 (2015), pp. 463–478.
- [13] A. Zizin, O. Lammel, M. Severin, H. Ax, and M. Aigner, *Development of a jet-stabilized low-emission combustor for liquid fuels*, Proceedings of ASME Turbo Expo (2015).
- [14] J.D. Gounder, A. Zizin, O. Lammel, M. Rachner, M. Aigner, and S.R. Kulkarni, *Experimental and numerical investigation of spray characteristics in a new FLOX[®] based combustor for liquid fuels for micro gas turbine range extender (MGT-REX).*, 52nd AIAA/SAE/ASEE Joint Propulsion Conference, 2016 (2016).
- [15] C. Bolszo, *Investigation of Atomization, Mixing and Pollutant Emissions for a Microturbine Engine*, The UCI Undergraduate Research Journal (2005), pp. 13–22.

- [16] A. Giusti, J.A. Sidey, G. Borghesi, and E. Mastorakos, *Simulations of droplet combustion under gas turbine conditions*, *Combustion and Flame* 184 (2017), pp. 101–116.
- [17] M. Tanabe, T. Bolik, C. Eigenbrod, H.J. Rath, J. Sato, and M. Kono, *Spontaneous ignition of liquid droplets from a view of non-homogeneous mixture formation and transient chemical reactions*, *Symposium (International) on Combustion* 26 (1996), pp. 1637–1643.
- [18] S. Schnaubelt, O. Moriue, T. Coordes, C. Eigenbrod, and H.J. Rath Zarm, *Detailed numerical simulations of the multistage self-ignition process of n-heptane, isolated droplets and their verification by comparison with microgravity experiments*, *Proceedings of the Combustion Institute* 28 (2000), pp. 953–960.
- [19] R. Stauch, S. Lipp, and U. Maas, *Detailed numerical simulations of the autoignition of single n-heptane droplets in air*, *Combustion and Flame* 145 (2006), pp. 533–542.
- [20] G. Borghesi and E. Mastorakos, *Spontaneous ignition of isolated n-heptane droplets at low, intermediate, and high ambient temperatures from a mixture-fraction perspective*, *Combustion and Flame* 162 (2015), pp. 2544–2560.
- [21] A. Cuoci, A. Frassoldati, T. Faravelli, and E. Ranzi, *Numerical modeling of auto-ignition of isolated fuel droplets in microgravity*, *Proceedings of the Combustion Institute* 35 (2015), pp. 1621–1627.
- [22] V.Y. Basevich, A.A. Belyaev, S.N. Medvedev, V.S. Posvyanskii, F.S. Frolov, and S.M. Frolov, *Simulation of the autoignition and combustion of n-heptane droplets using a detailed kinetic mechanism*, *Russian Journal of Physical Chemistry B* 4 (2010), pp. 995–1004.
- [23] J.R. Yang and S.C. Wong, *On the suppression of negative temperature coefficient (NTC) in autoignition of n-heptane droplets*, *Combustion and Flame* 132 (2003), pp. 475–491.
- [24] N. Iki, O. Kurata, T. Matsunuma, T. Inoue, M. Suzuki, T. Tsujimura, and H. Furutani, *Micro Gas Turbine Firing Kerosene and Ammonia*, *Proceedings of ASME Turbo Expo* (2015).
- [25] Ansaldo Energia, *AE-T100 Natural Gas Micro Turbine* (2019). Available at <https://www.ansaldoenergia.com/business-lines/new-units/microturbines/ae-t100ng>.
- [26] P.A. Pilavachi, *Mini- and micro-gas turbines for combined heat and power*, *Applied Thermal Engineering* 22 (2002), pp. 2003–2014.
- [27] S.Y. Cho, R.A. Yetter, and F.L. Dryer, *A computer model for one-dimensional mass and energy transport in and around chemically reacting particles, including complex gas-phase chemistry, multicomponent molecular diffusion, surface evaporation, and heterogeneous reaction*, *Journal of Computational Physics* 102 (1992), pp. 160–179.
- [28] G. Borghesi and E. Mastorakos, *Autoignition of n-decane Droplets in the Low-, Intermediate-, and High-temperature Regimes from a Mixture Fraction Viewpoint*, *Flow, Turbulence and Combustion* 96 (2016), pp. 1107–1121.
- [29] S. Liu, J.C. Hewson, J.H. Chen, and H. Pitsch, *Effects of strain rate on high-pressure nonpremixed n-heptane autoignition in counterflow*, *Combustion and Flame* 137 (2004), pp. 320–339.
- [30] R.W. Bilger, *The structure of turbulent nonpremixed flames*, *Symposium (International) on Combustion* 22 (1989), pp. 475–488.
- [31] R.W. Bilger, S.H. Stårner, and R.J. Kee, *On reduced mechanisms for methane-air combustion in nonpremixed flames*, *Combustion and Flame* 80 (1990), pp. 135–149.
- [32] D.G. Goodwin, R.L. Speth, H.K. Moffat, and B.W. Weber, *Cantera: An Object-oriented Software Toolkit for Chemical Kinetics, Thermodynamics, and Transport Processes Version 2.4.0* (2018). Available at <https://www.cantera.org>.
- [33] A. Millán-Merino, E. Fernández-Tarrazo, and M. Sánchez-Sanz, *Numerical analysis of the autoignition of isolated wet ethanol droplets immersed in a hot and humid air atmosphere*, *Combustion and Flame* 226 (2021), pp. 42–52.
- [34] Y.C. Liu, Y. Xu, M.C. Hicks, and C.T. Avedisian, *Comprehensive study of initial diameter effects and other observations on convection-free droplet combustion in the standard atmosphere for n-heptane, n-octane, and n-decane*, *Combustion and Flame* 171 (2016), pp. 27–41.
- [35] C.K. Law, *Asymptotic theory for ignition and extinction in droplet burning*, *Combustion*

- and Flame 24 (1975), pp. 89–98.
- [36] C.K. Westbrook, *Chemical kinetics of hydrocarbon ignition in practical combustion systems*, Proceedings of the Combustion Institute 28 (2000), pp. 1563–1577.